Plasma Chemistry and Plasma Processing
https://doi.org/10.1007/s11090-023-10438-4

ORIGINAL PAPER

# Numerical Simulation of the Voltage–Current Characteristic of an Atmospheric Pressure Discharge: The Glow-to-Arc Transition

**E. Cejas**[1] · **L. Prevosto**[1] · **F. O. Minotti**[2,3]

Received: 30 October 2023 / Accepted: 7 December 2023


**Abstract**
The glow-to-arc transition of a convection-stabilized atmospheric pressure air discharge is numerically investigated. Two separate models are considered: a one-dimensional axisymmetric time-dependent fluid model of the positive column, describing the thermal-instability, and a sheath model of a cold cathode describing the field-emission instability, which must then be properly matched together. The fluid model considers the most important chemical reactions in air plasma, including thermal ionization in atomic collisions. The radial electric field in the plasma is obtained from the Poisson equation. The voltage–current characteristic of the discharge is simulated for a time-varying current up to 300 mA. It is found that at some critical value slightly above 200 mA, the contraction of the positive column arises from a vibrational–translational energy relaxation. The subsequent increases in the discharge current density in the positive column drive in turn a field-emission instability in the cathode, which is accompanied by a large voltage drop. Simulation results are validated against available experimental data.

**Keywords** Glow-to-arc transition · Thermal instability · Field-emission instability · Numerical simulation · Voltage–current characteristic

## Introduction

It is widely accepted that in an atmospheric pressure glow-type discharge in the intermediate-current regime [1–4], the discharge structure is consistently contracted, resulting in a relatively high-gas temperature. However, despite this contraction, the discharge remains quit far from

✉ E. Cejas
cejasezequiel87@gmail.com

[1] Grupo de Descargas Eléctricas, Departamento Ing. Electromecánica, Facultad Regional Venado Tuerto, CONICET, Universidad Tecnológica Nacional, Laprida 651, Venado Tuerto, Santa Fe, Argentina

[2] Departamento de Física, Facultad de Ciencias Exactas y Naturales, Universidad de Buenos Aires, Buenos Aires, Argentina

[3] Instituto de Física Interdisciplinaria y Aplicada (INFINA), CONICET–Universidad de Buenos Aires, Buenos Aires, Argentina

Published online: 03 January 2024

kinetic equilibrium. This discharge can be considered as a 'hybrid' or filament discharge [5], sharing some common features with (diffusive) glow and (thermal) arc discharges [2, 4]. Additionally, it has been observed that at atmospheric pressure, a raising in the discharge current can disturb the discharge stability. This disturbance leads to the emergence of inhomogeneous modes caused by instabilities, which ultimately initiate the transition to an arc discharge, i.e., the glow-to-arc transition [5, 6].

According to the recent review work [7], there is still no wide consensus on the causes that lead to instability. Phenomena in the cathode region (characterized by large electric field values in self-sustained discharges) as well as processes in the plasma itself can contribute to this transition [8, 9]. There are at least two recognized (linked) mechanisms resulting in the glow-to-arc transition for a discharge operating with a cold cathode: (i) the so-called thermal instability, which causes contraction and thermalization of the discharge; and (ii) field-emission instability, which causes a shift from ion-impact emission to field-emission of electrons from the cathode surface [5].

Although constriction phenomena in atmospheric pressure discharges have been intensively investigated experimentally (see, e.g., [10]), the number of numerical investigations reported in the literature is not extensive. Numerical studies have been conducted principally at moderate pressure ($p = 50$–$500$ Torr) in atomic [11] as well as in molecular gases [12–14]. However, because those simulations do not include both thermal ionization reactions and cathode phenomena, they cannot simulate the transition to the arc phase. More recently [15] also a numerical investigation of a DC discharge in atmospheric pressure nitrogen gas in a tube with a thermionic cathode was developed under the one-dimensional approach. The model simulates several stages of the discharge, spanning from the Townsend to the arc regime in the current density range of $10^{-1}$–$10^{3}$ A/cm$^2$. The results suggest that the main mechanism of gas heating is vibrational–translational relaxation, accompanied by energy release in chemical reactions. At present there is no published numerical investigation involving both the phenomena in the cathode-sheath and the processes in the plasma that lead to the arcing transition of an air discharge at atmospheric pressure.

In the present study, a one-dimensional axisymmetric time-dependent fluid model is used to simulate a convection-stabilized atmospheric pressure air glow-type discharge. The elementary processes occurring within the positive column which are responsible for the thermalization of the discharge are examined. The model is coupled to an extended fluid model of the high-pressure cathode-sheath in a cold cathode [16] which accounts for the field-emission instability. The current–voltage characteristic of the discharge is investigated up to 300 mA. Simulation results are validated against available experimental data.

## Numerical Model

Two separate models are considered: a one-dimensional axisymmetric time-dependent fluid model describing the thermal-instability in the positive column, and a sheath model of a cold cathode describing the field-emission instability.

## Plasma Model

The discharge simulations were conducted for experimental conditions like those used in [2]. The discharge is generated between two flat copper electrodes aligned vertically and separated by an atmospheric air gap of $L = 3$ mm. The cathode is cooled with water. The polarity of the electrodes is set using a full-wave semiconductor rectifier bridge without a filter located in the secondary side of the high-voltage AC power transformer (25 kV, 50 Hz) with high-stray reactance ($95.3 \pm 0.5$ kΩ). The impedance of the transformer provides negative feedback between the discharge current and voltage without the use of external ballasts. The stray capacitance of the circuit (due to the wiring and electrodes geometry) is $C \approx 30$ pF. The discharge current $I$ is regulated through a variable autotransformer located in the primary circuit. The voltage $V$ of the discharge was measured using a high-voltage probe (Tektronix P6015A, 1000X, 3pf, 100 MΩ) connected to an oscilloscope (Tektronix TDS 2004C with a sampling rate of 1 GS/s and an analogical bandwidth of 70 MHz), while the discharge current was inferred through a 100 Ω shunt resistor. Note that the measured current not only contains the conduction (plasma) current, but also the small displacement current derived by the parallel stray capacitance. The electrode surfaces were polished between successive discharge ignitions to remove any contaminant from the electrodes.

A one-dimensional approach, in which the dependence of the plasma parameters is only on the radial coordinate $r$, is used to simulate the positive column of a convection-stabilized discharge in atmospheric pressure air as in [2]. For such conditions (gap lengths larger than 1 mm, much larger than typical discharge radii of the order of 0.1 mm) the radial gradients of the discharge parameters considerably exceed those along the discharge and the heat losses to the electrodes due to thermal conduction are negligible small [17]. However, the weak longitudinal (along the axis of the vertical column) flow effects caused by natural convection were considered.

The model includes time-dependent continuity equations for neutral species, ions, and electrons,

$$\frac{\partial [n_k]}{\partial t} + \frac{1}{r}\frac{\partial}{\partial r}\left(r\Gamma_k\right) = S_k - \frac{[n_k]}{\tau}, \tag{1}$$

in the drift–diffusion approximation [5],

$$\Gamma_{\mathrm{k}} = \mathrm{sgn}\left(q_{\mathrm{k}}\right)[n_{\mathrm{k}}]\mu_{\mathrm{k}}E_{\mathrm{r}} - D_{\mathrm{k}}\frac{\partial [n_{\mathrm{k}}]}{\partial r}. \tag{2}$$

In these equations, the subscript $k$ refers to the $k$-th species, being $[n_k]$ its corresponding number density. $D$ is the diffusion coefficient, $\mu$ the particle mobility, $q$ the electric charge, $E_{\mathrm{r}}$ the strength of the radial electric field, and $\tau$ the timescale of convection flow. The diffusion coefficients of neutral species are obtained from data at 300 K [18] and corrected by gas temperature [19]. The mobilities of charged particles are obtained from [20–22]. The diffusion coefficients of charged particles are obtained from the corresponding mobilities through the Einstein relation. The term $S$ represents the rate of production and destruction (negative in this case) of the species $k$ due to the reaction $i$.

The average vibrational energy $\varepsilon_{\mathrm{V}}$ of the $N_2$ molecule and the average translational energy of the neutral species (gas) are described through the corresponding energy balance equations,

$$\frac{\partial\left(\left[\mathrm{N_2}\right]\varepsilon_\mathrm{V}\right)}{\partial t}-\frac{1}{r}\frac{\partial}{\partial r}\left(rD\frac{\partial\left(\left[\mathrm{N_2}\right]\varepsilon_\mathrm{V}\right)}{\partial r}\right)=\eta_\mathrm{V}\sigma E_\mathrm{z}^2-\left[\mathrm{N_2}\right]\frac{\varepsilon_\mathrm{V}-\varepsilon_\mathrm{V}\left(T_\mathrm{g}\right)}{\tau_\mathrm{VT}}-\frac{\left[\mathrm{N_2}\right]\varepsilon_\mathrm{V}-\left[\mathrm{N_2}\right]_0\varepsilon_\mathrm{V}\left(T_0\right)}{\tau}, \tag{3}$$

$$\frac{\partial}{\partial t}\left(T_\mathrm{g}\sum_\mathrm{k}\left[n_\mathrm{k}\right]c_\mathrm{pk}\right)-\frac{1}{r}\frac{\partial}{\partial r}\left(r\kappa\frac{\partial T_\mathrm{g}}{\partial r}\right)=\eta_\mathrm{T}\sigma E_\mathrm{z}^2+\left[\mathrm{N_2}\right]\frac{\varepsilon_\mathrm{V}-\varepsilon_\mathrm{V}\left(T_\mathrm{g}\right)}{\tau_\mathrm{VT}}+Q_\mathrm{R}-\frac{T_\mathrm{g}\sum_\mathrm{k}\left[n_\mathrm{k}\right]c_\mathrm{pk}-T_0\sum_\mathrm{k}\left[n_\mathrm{k}\right]_0c_\mathrm{pk}}{\tau}. \tag{4}$$

The average vibrational energy of the nitrogen molecule and its vibrational temperature $T_\mathrm{v}$ are related through the equation $\varepsilon_\mathrm{V}=q\hbar\omega/\left[\exp\left(q\hbar\omega/\left(k_\mathrm{B}T_\mathrm{V}\right)\right)-1\right]$. Here, $\hbar\,\omega$ is the vibrational quantum of the $N_2$ molecule (=0.29 eV) and $\varepsilon_\mathrm{V}\left(T_\mathrm{g}\right)$ its equilibrium vibrational energy value for $T_\mathrm{v}=T_\mathrm{g}$ [12, 17, 19, 23]. $k_\mathrm{B}$ is the Boltzmann constant. The vibration–translation relaxation time (V–T), $\tau_\mathrm{VT}$, considers the relevant V–T relaxation processes in nitrogen–oxygen mixtures [19]. The dependence of the rate of V–T relaxation by O atoms on the gas temperature is taken from [24]. $\sigma$ is the electrical conductivity ($=q\,[n_\mathrm{e}]\,\mu_\mathrm{e}$) and $E_\mathrm{z}$ is the axial component of the electric field strength. The coefficients $\eta_\mathrm{V}$ and $\eta_\mathrm{T}$ represent the fraction of electronic energy transferred to the vibrational and translational modes, respectively. $Q_\mathrm{R}$ is the energy transfer to the gas due to the fast electronic–translational relaxation (E–T) [24, 25] in reactions of electron-impact predissociation and electron–ion recombination. $c_\mathrm{pk}$ is the heat capacity of the neutral species $k$ ($=7/2\,k_\mathrm{B}$ for diatomic molecules, $8/2\,k_\mathrm{B}$ for triatomic molecules, and $5/2\,k_\mathrm{B}$ for atoms) and $\kappa$ is the translational component of the heavy particles thermal conductivity [26].

In Eqs. (1), (3), and (4), the last term on their right-hand sides accounts for the transport along the axial coordinate $z$ due to the weak longitudinal flow effects caused by natural convection [5, 27]. The variation of $\tau$ with $r$ is estimated by assuming that the axial velocity of the gas follows the analytical expression [28]:

$$v(r)=\sqrt{\frac{2g\left(\rho_0(r)-\rho(r)\right)z}{\rho(r)}}, \tag{5}$$

where $g$ is gravitational acceleration, and $\rho$ the gas density. This simple approximation based on the Bernoulli's equation agrees well with the variation of $v$ with $r$ and discharge current $I$ found in a two-dimensional numerical simulation of a natural convection-stabilized low-current discharge in atmospheric pressure air [17]. The subscript 0 refers to the radial distribution of the corresponding quantity at $T_0=300$ K.

The coupling of the fluid equations with Poisson's equation guarantees the self-consistent treatment of charged particle transport. The strength of the radial electric field, $E_\mathrm{r}$ is calculated by means of the electrostatic approximation,

$$E_\mathrm{r}=-\frac{\partial\varphi}{\partial r}, \tag{6}$$

where $\varphi$ is the corresponding electrostatic potential obtained from the Poisson's equation

$$-\frac{1}{r}\frac{\partial}{\partial r}\left(r\frac{\partial \varphi}{\partial r}\right)=\frac{1}{\varepsilon_0}\sum_{\mathrm{k}} q_{\mathrm{k}}\left[n_{\mathrm{k}}\right], \tag{7}$$

where $\varepsilon_0$ is the vacuum permittivity.

The axial electric field strength in the discharge column is obtained from Ohm's law,

$$E_z=\frac{I_p}{2\pi\int_0^R \sigma(r) r dr}, \tag{8}$$

where $\sigma$ is electrical conductivity and $I_{\mathrm{p}}$ the conduction current through the discharge.

The kinetic scheme used in this model is based on that proposed in [23] and used in [2] and [17]. A total of 40 reactions are considered in the model, which are presented in Appendix 1 (Table 1). Thus, Eq. (1) was solved for a scheme that included reactions involving neutral molecular and atomic species ($N_2$, $O_2$, NO, $O_3$, $N_2O$, $NO_2$, N and O), ions ($NO^+$, $N_2^+$, $O_2^+$, $O^+$, O–, $O_{2-}$ y $O_{3-}$) and electrons (e). The number density of the dominant species $N_2$ was determined by the constancy of the pressure ($p=10^5$ Pa). Meanwhile, the density of $O_2$ was calculated from the *N* and *O* conservation considering the initial gas composition.

The transport and reaction coefficients of electrons are determined as functions of the local reduced electric field $E_z/N$ (where *N* is the total neutral density) by using a Boltzmann solver [29]. This approach, which is typically satisfied in molecular plasmas at atmospheric pressure (e.g., [5, 19]), has been successfully employed to simulate the contraction of a glow-type discharge in nitrogen and air gases [12, 14, 30]. The reaction coefficients of electrons are calculated for the mixture $N_2$:$O_2$=4:1 [23] (they depend on the mixture composition only slightly [31]). The corresponding cross-section data are taken from [32] and [33]. The 'effective' electron temperature, $T_{\mathrm{e}}$, is assumed to be 2/3 of the mean electron energy. The values of $\eta_{\mathrm{T}}$ and $\eta_{\mathrm{V}}$ are determined as functions of the $E_z/N$ values. The parameter $\eta_{\mathrm{T}}$ in (4) accounts not only for the electron energy that goes directly into gas heating through elastic collisions, but also those of rotational excitation of the $N_2$ and $O_2$ molecules, as well as of vibrational excitation of the $O_2$ molecules, which fast relax into gas heating through neutral collisions. Additionally, the reaction rates for high-threshold electron impact reactions were corrected to account for the deformation in the electron energy distribution function calculated for the vibrationally non-excited conditions through the factor $F=\exp\left(Cz/\left(E_z/N\right)^2\right)$, where $C=6.5\times10^3$ Td and $z=\exp\left(-\hbar\omega/k_{\mathrm{B}}T_V\right)$ [5, 19, 23]. Furthermore, the enhancement in the thermal dissociation rate of $N_2$ under non-equilibrium conditions was considered through the Losev β model [34, 35].

The rates of the processes of thermal ionization in atomic collisions (R7) and of electron recombination with $NO^+$ ions (R8) were taken from various authors [36–40]. The presented results were obtained for rates (R7) and (R8) taken from [38] and [40] respectively. However, the influence of the relatively large uncertainties in the reaction coefficients of processes (R7) and (R8) on the critical value at which the plasma contraction occurs is also assessed (see below).

The model radial domain is uniformly discretized into a 200-cell grid. The radius *R* of the domain was taken large enough so that the variation of *R* as well as the boundary conditions at $r=R$ have a negligible influence on the model calculations. At the discharge axis ($r=0$) rotational symmetry conditions ($\partial/\partial r=0$) are assumed, while at $r=R$ free boundary conditions ($\partial/\partial r=0$) are considered for all plasma quantities except for the gas temperature and potential, for which $T_{\mathrm{g}}$ ($r=R$)$=T_0$ and $\varphi(r=R)=0$, is used.

At the initial instant, the radial profile of the gas temperature was specified, and the densities of the main neutral species were assumed to be equal to their equilibrium values. The initial distributions of charged particles as well as the gas temperature were described by a Gaussian-like radial profile. The specific values used for these initial conditions have no significant impact on the simulation results. Because of the stiffness of the equations, the temporal step was $1.0\times10-^{10}$ s during the glow-type phase but had to be strongly reduced to $1.0\times10-^{15}$ s at the early stages of the arcing transition due to the shortening of time scales associated with different plasma processes which reduce the time step needed for an accurate numerical integration.

Balance Eqs. (1), (3), and (4) are solved using the implicit Crank–Nicholson scheme [41]. The drift–diffusion fluxes in (1) were approximated using the exponential difference scheme [42]. For 200 cells, calculations demonstrate that the ratio of potential drop between two adjacent cells to the local electron temperature remains significantly lower than unity (less than $10^{-2}$) throughout the entire radial coordinate, thus providing confidence on the accuracy of using the exponential difference scheme [43]. Furthermore, the accuracy of the results was verified by repeating the simulation with a grid consisting of 600 cells (i.e., by reducing the radial thickness of the cells by a factor of 3) at the expense of a significant increase in computational cost. The differences found in the radial distributions of the different plasma variables were less than 5%.

The Poisson Eq. (7) was solved by the relaxation method based on the Gauss–Seidel iteration scheme with successive over-relaxation [41].

The experimentally inferred current and voltage waveforms of the discharge are shown in Fig. 1. At these experimental conditions, the discharge was unstable. Figure 1 shows that at some critical value slightly above 200 mA the discharge voltage suddenly drops as the discharge regime changes to an arc, and then rises again for some lower current value when the discharge returns to a glow. Similar voltage disturbances have been previously observed [44, 45].

The inclusion of the external circuit into the model is not necessary because the temporal evolution of the axial electric field in the discharge is self-consistently determined from (8) for the measured current data. It should be noted that the discharge current waveform under the condition considered [2] is almost independent of the discharge parameters since the current is mainly controlled by the high impedance of the external circuit transformer. On the other hand, the discharge voltage (or axial electric field) reflects the elementary processes that occur within the plasma column as well as in the near-electrode sheaths (mostly the cathode). Calculations show that the displacement current through the small stray capacitance of the circuit is negligibly small compared to the conduction current, even during the arcing transition when it reaches a value $<0.1$ mA.

## Cathode Model

A one-dimensional fluid model is used to simulate the underlying processes leading to the field-emission instability at the Cu cathode of an atmospheric pressure air discharge. The model aims to study the glow-to-arc transition in which the field electron emission (given by the Fowler–Nordheim equation) replaces secondary emission due to the intensification of the non-local ionization processes within the cathode-sheath as the current density increases. The model simulates the cathode fall voltage–cathode current density ($V_C$–$j_C$) characteristic within the broad cathode current density range of 1 to $10^2$ A/cm$^2$;

highlighting three different stages of a typical self-sustained quasi-stationary discharge: from the normal glow discharge, through abnormal glow discharge, to the onset of the arcing transition. A detailed description of the model can be found in [16].

The specific conditions on the cathode surface have a strong effect on determining the critical value of the cathode current density at which the field-emission instability develops according to the Fowler–Nordheim equation. For the conditions considered in [16] (a cathode work function $\varphi_C = 2$ eV and a field enhancement factor $\beta = 15$) the model predicts that the field-emission instability arises when the cathode current density is larger than a critical value of 10 A/cm$^2$. Experimental data [2, 45, 46] indicates that the cathode current density is around 9–11 A/cm$^2$ for discharge currents in the range of 100–200 mA. As this current range is close to the critical current value measured for the glow-to-arc transition (about 210 mA, as shown in Fig. 1), the data appear to support that field-emission instability arises for a cathode current density larger than 10 A/cm$^2$.

It should be noted that the experimental current range shown in Fig. 1 does not include the threshold required for the formation of a hot arc spot, which is greater than 500 mA for Cu cathode [47]. The latter is characterized by intensive cathode evaporation and cathode temperature high above the boiling point. This arc takes place almost independent on the environment pressure [5]. These conditions cannot be described within the frame of the cathode-sheath model [16].

To join both models, the (average) current density in the cathode $j_C$ (which is the input of the cathode model) should be linked with the radial profile of the current density simulated in the positive column by the fluid model,

$$j_C = \frac{j(r=0)}{A_C/A^*}, \tag{9}$$

where $j(r=0)$ is the axial value of the current density in the positive column corresponding to each measured discharge current value, $A_C$ is the area of the cathode, and $A^*$ is the effective discharge area (defined by $I/j(r=0)$). Unlike low-pressure glow discharges that have the same current density in the positive column as in the negative glow (i.e., $A_C \approx A^*$), at atmospheric pressure the current density in the positive column is typically higher than that of the cathode. The value of the ratio $A_C/A^*$, was properly chosen so that the thermal-instability in the positive column as well as the field-emission instability in the cathode occur simultaneously for some critical value of the discharge current.

Anode phenomena are unessential to describe the glow-to-arc transition [5]. The minor anode fall was included in the calculations as a constant value. Since no data at atmospheric pressure air can be found in the literature, it was estimated by extrapolating the linear pressure dependence of the anode fall in the air pressure range of 20–200 Torr reported in [5] to 760 Torr.

Within the frame of the coupled model (cathode and plasma) the discharge voltage is determined by adding the voltage drop across the positive column ($=E_z \times L$), which is calculated by the plasma model through (8) for each value of the measured discharge current waveform, together with the cathode fall, which is calculated by the cathode model from the $V_C$–$j_C$ characteristic using (9); and the anode fall as a constant value.

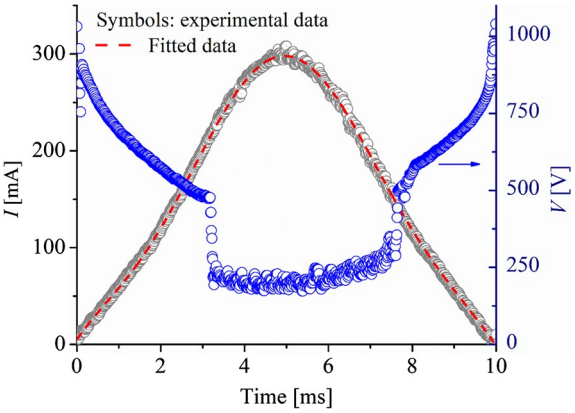


**Fig. 1** Current and voltage waveforms of the discharge. At a critical value slightly above 200 mA a voltage drop is observed as the discharge momentarily changed to an arc and then reverted to a glow

## Numerical Results and Comparison with Experimental Data

Figure 2 shows axial values of electron temperature, gas temperature, and vibrational temperature of the $N_2$ molecules versus the discharge current. As the discharge current increases the gas temperature increases, thus leading to a significant decrease in the departure between the vibrational and gas temperatures. This can be attributed to the strong dependency of the V–T energy relaxation rate on the gas temperature. Most of the electron power ($\eta_V \sim 0.82$–$0.90$) is transferred to the vibrational modes of $N_2$ molecules, according to the values of the mean electron energies ($<1$ eV). At some critical current value slightly above 200 mA, a significant increase in the vibrational temperature (within a time of the order of 100 μs) results in a further rise in the gas temperature through intensification of V–T relaxation processes, mainly by collisions between $N_2$ molecules and O atoms. The gas undergoes rapid heating at a rate of $5\times10^6$ K/s, eventually reaching a temperature of around 5800 K. The vibrational temperature experiences also a significant increase at a rate of approximately $1\times10^7$ K/s, bringing it close to the electron temperature due to the substantial increase in electron density (as shown in Fig. 4). However, this energy is not completely transferred to the gas due to an incomplete V–T relaxation. This high rate of increase in gas temperature indicates the onset of thermal instability, resulting in

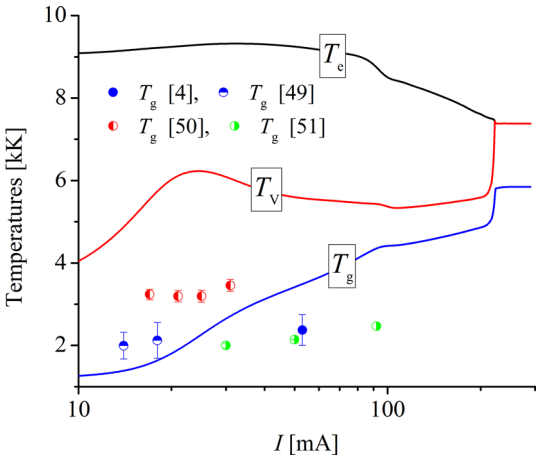


**Fig. 2** Axial distribution of the electron ($T_e$), vibrational ($T_V$), and gas ($T_g$) temperatures versus the discharge current. Available experimental data for the gas temperature are also presented

the thermalization and contraction of the discharge column [5, 48]. The fast E–T relaxation also plays a role during the contraction of the discharge (contributing to about 10% of the V–T relaxation), mainly through electron–ion recombination. Experimental data [4, 49–51] are also shown in Fig. 2. Considering that there is a limited amount of experimental data available for the conditions considered, the agreement with the simulations is reasonably good.

Figure 3 shows the axial values of the number density of several neutral species versus the discharge current. Up to a current value of 60 mA, the primary production of N and O atoms is attributed to vibrational non-equilibrium thermal dissociation of $N_2$ molecules (R12) and electron-impact dissociation of $O_2$ molecules (R6), respectively. The destruction of O atoms gradually changes from the three-body recombination (R18) and (R19) to the reaction (R26), which becomes the dominant mechanism. The mechanism of destruction of N atoms is primarily governed by (R25), but then switches to (R24). The production of NO molecules is mainly governed by (R25) up to a current value of 60 mA, above which the dominant mechanism becomes (R26). The destruction processes shift from ion conversion reaction (R39) to reaction (R24). Some underestimations in the neutral densities of O (as well as NO) may be expected for low current values because the O atoms are also produced via quenching of excited states of $N_2$ molecules. Above 60 mA the production of O atoms is mainly due to (R24), while the formation of N atoms is governed by (R26). For currents higher than 90 mA the reactions (R24) and (R26) are mutually balanced. For currents higher than 200 mA ($T_g > 5000$ K), which corresponds to the thermalization of the discharge, the densities of neutral particles are close to their corresponding equilibrium values [52].

Figure 4 shows the axial values of the number densities of several ions and electrons in the plasma versus the discharge current, while Fig. 5 shows the corresponding time-evolution of the electron number density. For currents higher than 20 mA the dominant ion is $NO^+$. The numerical densities of negative oxygen ions resulting from electron attachment is negligible compared to that of $NO^+$ ions (and hence negligible in comparison to the electron number density). This implies that electron attachment does not play a substantial role in this discharge. For discharge currents greater than 200 mA, the electron density undergoes a sharp increase of approximately one order of magnitude when the discharge contraction occurs. This is also highlighted in Fig. 5, where the discharge contraction

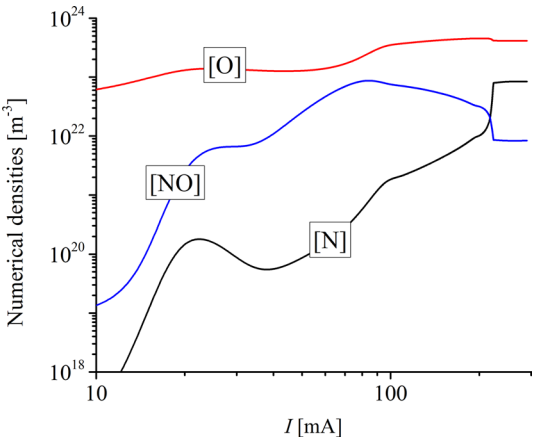


**Fig. 3** Axial number density of neutral species (N, O, and NO) versus the discharge current

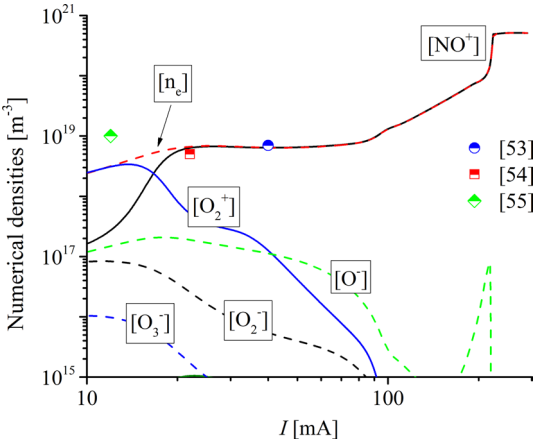


**Fig. 4** Axial distribution of several mechanisms involved in the production and loss of electrons versus the discharge current

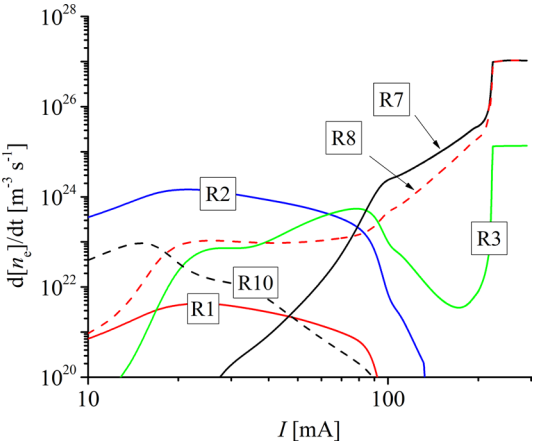


**Fig. 5** Axial distributions of the number density of several ions and electrons versus the discharge current. Available experimental data are also presented

(occurring at about 3.2 ms according to the current waveform given by the external circuit) is indicated by an arrow. The electron density then stabilizes again at a high value (of about $5\times10^{20}$ m$^{-3}$) due to the increase in the recombination rate favored by the decrease in electron temperature. The electron density in the arc phase approaches its equilibrium value corresponding to the gas temperature [52]. The simulated electron density shows good agreement with available experimental data [53–55].

Figure 6 shows the different mechanisms involved in the production and loss of electrons at the axis of the plasma column versus the discharge current. The changes in the ionization kinetics in the glow phase as the discharge current increases are well known in the literature (e.g., [2, 23, 31]). The dominant charge production mechanism undergoes a progressive change with increasing discharge current (or gas temperature), from direct electron-impact to thermal ionization. For currents higher than 80 mA, when the gas temperature is rather high ($T_g > 4200$ K), the dominant process of production of electrons is the thermal ionization in atomic collisions (R7). For low discharge current values, some imbalance in the ionization processes is observed, mainly caused by the time-variation of the discharge current with a timescale of 10 ms (as shown in Fig. 1). Indeed, for currents

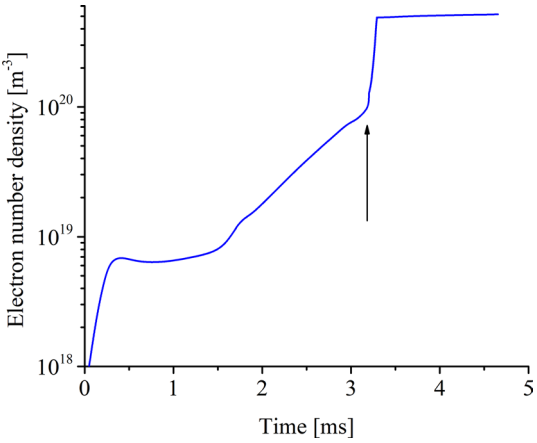


**Fig. 6** Time-evolution of the number electron density according to the discharge current waveform shown in Fig. 1. The arrow indicates the discharge contraction

higher than 200 mA a sort of detailed balance is observed between thermal ionization (R7) and dissociative recombination (R8) due to the reduction of the electron–ion recombination timescale caused by the rapid growth of the electron density.

Figure 7 shows the axial values of the reduced electric field (1 Td ≡ $10^{-21}$ V m$^2$) versus the discharge current. For currents higher than 80 mA ($T_g > 4200$ K) the thermal ionization (R7) leads to a sharp drop in $E_z/N$ to ~ 10 Td. This small value of the reduced electric field favors kinetic equilibrium in the plasma column as shown in Fig. 2. The decrease in the electron temperature (linked by the reduction in $E_z/N$ through the local field approximation) is expected because the production rate of electrons through the process (R7) does not depend on $T_e$.

Figure 8 shows the axial component of the electric field versus the discharge current. The contraction of the plasma column is marked by an abrupt decline in the axial electric field, which is accompanied by a significant increase in electron density (Fig. 5 and 6). The simulated electric field is in good arrangement with available experimental data [2, 45, 55, 56].

Figure 9 shows the current density at the discharge axis and the cathode-fall voltage $V_C$ versus the discharge current. The contraction of the plasma column is marked by an abrupt

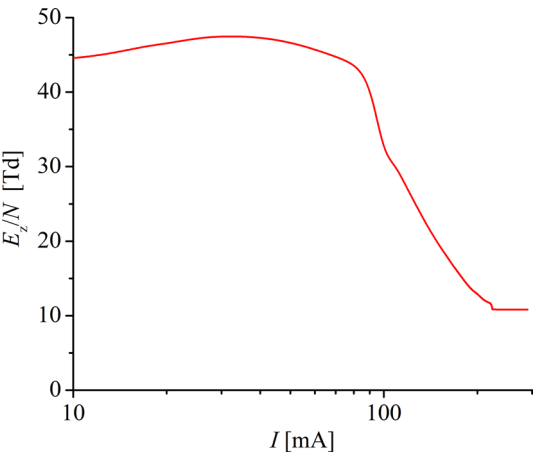


**Fig. 7** Axial distribution of the reduced electric field versus the discharge current

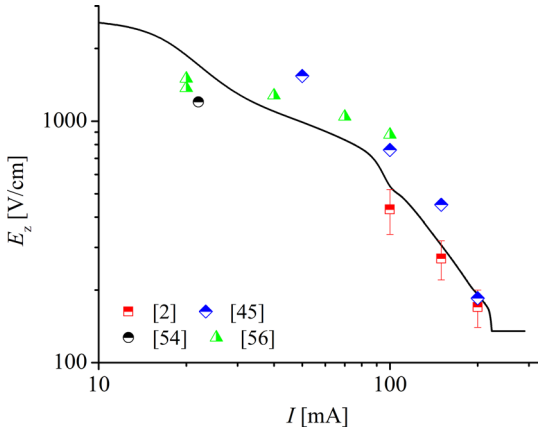


**Fig. 8** Axial component of the electric field versus the discharge current. Available experimental data are also presented

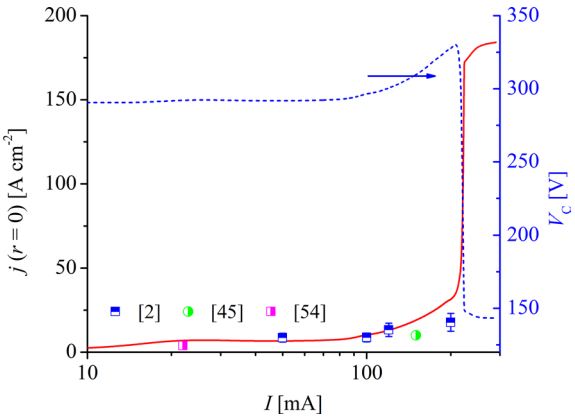


**Fig. 9** Current density at the axis of the positive column and cathode-fall versus the discharge current. The contraction of the plasma column is marked by an abrupt increase in the current density accompanied by a similar decrease in the cathode-fall. Available experimental data for the glow-phase regime is also presented

increase in the current density from ~35 A cm$^{-2}$ to over 170 A cm$^{-2}$. This contraction induces in turn the field-emission instability in the cathode leading to a sharp decrease of the cathode-fall to ~140 V. This value of the cathode-fall is greater than that corresponding to a high-current arc (~10 V), but lower than that of a glow with a Cu cathode (~360 V) [2]. Such a chain of causal events, leading to the arcing transition, occurs for a critical current density in the cathode of ~10 A/cm$^2$. This corresponds to the ratio $A_C/A^* \sim 3.5$. However, because the current density in the positive column sharply grows during contraction, the simulation results are not very sensitive to the used value of the ratio $A_C/A^*$. Previous works [2, 45, 46] indicate that the ratio $A_C/A^*$ varies in the range 2–6 for the current regime of 100–200 mA. It is important to note that the radii of the emission discharge and the current discharge may not be equivalent, and their values, as well as their ratios, may depend on the experimental conditions [25, 27]. The simulated current density is in good agreement with available experimental data [2, 45, 54] for the glow-phase regime.

Figure 10 shows the radial distribution of the current density in the positive column for several discharge currents. For currents higher than 210 mA the development of the thermal instability in the positive column results in a rapid formation of a quasi-equilibrium hot narrow tube. The characteristic radius of the tube is in the same order as the length of the region where the electrons move through diffusion during its recombination lifetime.

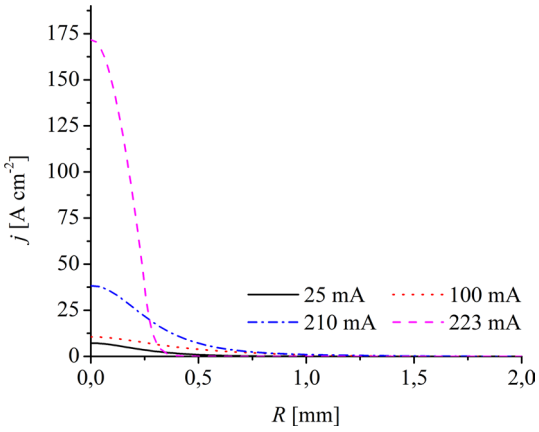


**Fig. 10** Radial distribution of the current density in the positive column for several discharge currents. The formation of a quasi-equilibrium hot narrow tube is observed at a critical current value above 210 mA

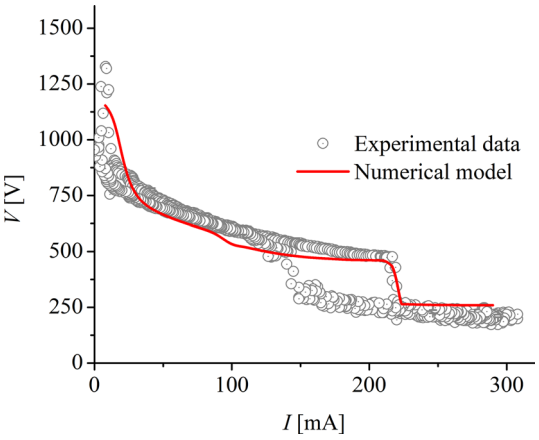


**Fig. 11** Voltage–current characteristic of the discharge. Symbols: experimental data, lines: calculations

Figure 11 shows the simulated and measured voltage–current characteristic curve of the discharge for the conditions depicted in Fig. 1. The discharge voltage follows the previously depicted changes in both the ionization mechanisms in the discharge column and the phenomena at the cathode as the discharge current increases. The agreement between the model and the experimental data is good. The relatively large uncertainties in the reaction coefficients of the processes of thermal ionization (R7) and dissociative recombination (R8) influence the critical value at which the plasma contraction occurs. Calculations show that the uncertainty in the critical current value caused by the uncertainties in the reaction coefficients of the processes of thermal ionization (R7) and dissociative recombination (R8) is within the range of 120–260 mA. This current range contains the measured value.

## Conclusions

The glow-to-arc transition of a convection-stabilized atmospheric pressure air discharge with a copper cathode was numerically investigated. The two interrelated key mechanisms resulting in the glow-to-arc transition were simulated. The calculations show that:

1. At some critical value slightly above 200 mA the contraction of the positive column arises. The gas temperature experiences a rapid increase at a rate of approximately $5 \times 10^6$ K/s, primarily attributed to the V–T relaxation process. Additionally, the electron number density undergoes a significant increase while the axial electric field decreases, leading to the thermalization of the discharge.
2. The subsequent increase in the discharge current density in the positive column drives in turn a field-emission instability in the cathode when its current density reaches some critical value above 10 A/cm$^2$. This transition is accompanied by a large voltage drop.
3. The simulated voltage–current characteristic curve agrees well with experimental data. The uncertainty in the critical discharge current value is within the range of 120–260 mA, caused by the uncertainty in the rate coefficients that govern the ionization balance in the high-temperature air.

## Appendix 1

See Table 1.

**Table 1** List of reactions. $T_e$ and $T_g$ are in Kelvin

| No *i* | Reaction | Rate Coefficient ($m^3/s$ or $m^6/s$) | Refs |
|---|---|---|---|
| R1 | $e+N_2 \rightarrow e+e+N_2^+$ | $k_1 = f(E_z/N)$ | [29, 32] |
| R2 | $e+O_2 \rightarrow e+e+O_2^+$ | $k_2 = f(E_z/N)$ | [29, 32] |
| R3 | $e+NO \rightarrow e+e+NO^+$ | $k_3 = f(E_z/N)$ | [29, 33] |
| R4 | $e+O \rightarrow e+e+O^+$ | $k_4 = f(E_z/N)$ | [29, 33] |
| R5 | $e+N_2 \rightarrow e+N_2^*$ ($\Delta E = 13$ eV) $e+N+N$ | $k_5 = f(E_z/N)$ | [29, 32] |
| R6 | $e+O_2 \rightarrow e+O_2^*$ ($\Delta E = 6$ eV) $e+O+O$ | $k_6 = f(E_z/N)$ | [29, 32] |
| R7 | $N+O \rightarrow NO^+ + e$ | $k_7 = 2.33\times10^{-24}\, T_g^{1.5} \exp(-31{,}900/T_g)$ | [36] |
| | | $k_7 = 5.0\times10^{-17}\, T_g^{-0.5} \exp(-32{,}500\, T_g)$ | [37] |
| | | $k_7 = 2.6\times10^{-23}\, T_g^{1.43} \exp(-31{,}140/\, T_g)$ | [38] |
| | | $k_7 = 1.5\times10^{-21}\, T_g \exp(-32{,}000/\, T_g)$ | [39] |
| R8 | $e+NO^+ \rightarrow N+O$ | $k_8 = 1.1\times10^{-8}\, T_e^{-1.5}$ | [36] |
| | | $k_8 = 3.0\times10^{-9}\, T_e^{-1.5}$ | [37] |
| | | $k_8 = 2.3\times10^{-12}\, T_e^{-0.45}$ | [38] |
| | | $k_8 = 1.5\times10^{-11}\, T_e^{-0.65}$ | [39] |
| | | $k_8 = 4.0\times10^{-13}\, (300/T_e)^{1.5}$ | [40] |
| R9 | $e+N_2^+ \rightarrow N+N$ | $k_9 = 2.0\times10^{-13}\, (300/T_e)^{0.5}$ | [40] |
| R10 | $e+O_2^+ \rightarrow O+O$ | $k_{10} = 2.0\times10^{-13}\, (300/\, T_e)$ | [40] |
| R11 | $e+e+O^+ \rightarrow e+O$ | $k_{11} = 1.0\times10^{-31}\, (300/T_e)^{4.5}$ | [40] |
| R12 | $N_2+M \rightarrow N+N+M$<br>$M = N_2, O_2, NO$ | $k_{12} = 5\times10^{-14} \exp(-113{,}200/T_g)\, [1\, \exp(-3354/T_g)]$ | [31] |
| R13 | $N_2+M \rightarrow N+N+M$<br>$M = N, O$ | $k_{13} = 1.1\times10^{-13} \exp(-113{,}200/T_g)\, [1-\exp(-3354/T_g)]$ | [31] |
| R14 | $N+N+M \rightarrow N_2+M$<br>$M = N_2, O_2, NO, N, O$ | $k_{14} = 8.27\times10^{-46} \exp(500/T_g)$ | [31] |
| R15 | $O_2+M \rightarrow O+O+M$<br>$M = O_2$ | $k_{15} = 3.7\times10^{-14} \exp(-59{,}380/T_g)\, [1-\exp(-2240/\, T_g)]$ | [31] |

**Table 1** (continued)

| No *i* | Reaction | Rate Coefficient ($m^3/s$ or $m^6/s$) | Refs |
|---|---|---|---|
| R16 | $O_2+M \rightarrow O+O+M$<br>$M=O$ | $k_{16}=1.3\times10^{-13}\exp(-59{,}380/T_g)\,[1-\exp(-2240/T_g)]$ | [31] |
| R17 | $O_2+M \rightarrow O+O+M$<br>$M=N_2$, N, NO | $k_{17}=9.3\times10^{-15}\exp(-59{,}380/T_g)\,[1-\exp(-2240/T_g)]$ | [31] |
| R18 | $O+O+M \rightarrow O_2+M$<br>$M=N_2$ | $k_{18}=2.76\times10^{-46}\exp(720/T_g)$ | [31] |
| R19 | $O+O+M \rightarrow O_2+M$<br>$M=O_2$ | $k_{19}=2.45\times10^{-43}\,T_g^{-0.63}$ | [31] |
| R20 | $O+O+M \rightarrow O_2+M$<br>$M=O$ | $k_{20}=8.8\times10^{-43}\,T_g^{-0.63}$ | [31] |
| R21 | $NO+M \rightarrow N+O+M$<br>$M=N_2(X)$, $O_2$ | $k_{21}=8.7\times10^{-15}\exp(-76{,}000/T_g)$ | [31] |
| R22 | $NO+M \rightarrow N+O+M$<br>$M=O$, NO | $k_{22}=1.7\times10^{-13}\exp(-76{,}000/T_g)$ | [31] |
| R23 | $N+O+M \rightarrow NO+M$<br>$M=N_2$, $O_2$, O, NO | $k_{23}=1.76\times10^{-43}\,T_g^{-0.5}$ | [31] |
| R24 | $N+NO \rightarrow O+N_2$ | $k_{24}=1.0\times10^{-18}\,T_g^{0.5}$ | [40] |
| R25 | $N+O_2 \rightarrow O+NO$ | $k_{25}=1.1\times10^{-20}\,T_g\exp(-3150/T_g)$ | [40] |
| R26 | $O+N_2 \rightarrow N+NO$ | $k_{26}=1.3\times10^{-16}\exp(-38{,}000/T_g)$ | [31] |
| R27 | $O+NO \rightarrow N+O_2$ | $k_{27}=2.5\times10^{-21}\,T_g\exp(-19{,}500/T_g)$ | [31] |
| R28 | $e+O_2+O_2 \rightarrow O_2^-+O_2$ | $k_{28}=1.4\times10^{-41}\,(300/T_e)\exp(-660/T_g)\exp[700\,(T_e-T_g)/(\,T_e\,T_g)]$ | [40] |
| R29 | $e+O_2 \rightarrow O^-+O$ | $k_{29}=f\,(E_z/N)$ | [29, 32] |
| R30 | $O_2^-+O_2 \rightarrow O_2+O_2+e$ | $k_{30}=2.7\times10-16\,(T_g/300)^{0.5}\exp(-5590/Tg)$ | [40] |
| R31 | $O_2^-+O \rightarrow O_3+e$ | $k_{31}=1.5\times10^{-16}$ | [40] |
| R32 | $O^-+N_2 \rightarrow N_2O+e$ | $k_{32}=9.0\times10^{-19}$ | [40] |
| R33 | $O^-+O \rightarrow O_2+e$ | $k_{33}=5.0\times10^{-16}$ | [40] |
| R34 | $O^-+NO \rightarrow NO_2+e$ | $k_{34}=2.6\times10^{-16}$ | [40] |
| R35 | $O_3^-+O \rightarrow O_2+O_2+e$ | $k_{35}=3.0\times10^{-16}$ | [40] |

**Table 1** (continued)

| No *i* | Reaction | Rate Coefficient ($m^3/s$ or $m^6/s$) | Refs |
|---|---|---|---|
| R36 | $O^- + O_2 + M \rightarrow O_3^- + M$<br>$M = N_2, O_2$ | $k_{36} = 1.1 \times 10^{-42} (300/T_g)$ | [40] |
| R37 | $O^+ + N_2 \rightarrow NO^+ + N$ | $k_{37} = (1.5\text{–}2.0 \times 10^{-3} T_g + 9.56 \times 10^{-7} T_g^2) \times 10^{-18}$ | [57] |
| R38 | $N_2^+ + O_2 \rightarrow N_2 + O_2^+$ | $k_{38} = 6 \times 10^{-17} (300/T_g)^{0.5}$ | [40] |
| R39 | $O_2^+ + NO \rightarrow NO^+ + O_2$ | $k_{39} = 6.3 \times 10^{-16}$ | [57] |
| R40 | $X^- + Y^+ \rightarrow X + Y$<br>$X^- = O^-, O_2^-, O_3^-$<br>$Y^+ = N_2^+, O_2^+, NO^+, O^+$ | $k_{40} = 2.0 \times 10^{-13} (300/T_g)^{0.5}$ | [40] |

**Acknowledgements** This work was supported by grants from the Universidad Tecnológica Nacional (PID 8460, PID 8461 and PID 8568) and CONICET (PIP CONICET 11220200100459CO). L. P. and F. O. M. are members of the CONICET. E. C. thanks CONICET for their postdoctoral fellowships.

**Author contributions** E.C. and L.P. conceived, planned, and carried out the experiment; E.C., L.P., and F.O.M. developed the theoretical formalism; E.C. and F.O.M. developed, performed, and carried out the numerical simulations; E.C., L.P., and F.O.M. contributed to the interpretation of the results; writing—original draft preparation, E.C.; writing—review and editing, E.C, L.P., and F.O.M.; project administration, E.C., L.P.; funding acquisition, E.C., L.P.; All authors have read and agreed to the published version of the manuscript.

**Data Availability** The data that supports the findings of this study are available within the article.

## Declarations

**Conflict of interest** The authors have no competing interests to declare that are relevant to the content of this article.

**Ethical Approval** Not applicable.

## References

1. Giuliani L, Xaubet M, Grondona D, Minotti F, Kelly H (2013) Electrical studies and plasma characterization of an atmospheric pressure plasma jet operated at low frequency. Phys Plasmas. https://doi.org/10.1063/1.4812463
2. Prevosto L, Kelly H, Mancinelli B, Chamorro JC, Cejas E (2015) On the physical processes ruling an atmospheric pressure air glow discharge operating in an intermediate current regime. Phys Plasmas 1063(1):4907661
3. Kong C, Li Z, Alden M, Ehn A (2019) Thermal analysis of a high-power glow discharge in the flowing atmospheric air by combining Rayleigh scattering thermometry and numerical simulation. J Phys D Appl Phys. https://doi.org/10.1088/1361-6463/ab586f
4. Cejas E, Chamorro JC, Prevosto L (2022) Quantitative schlieren diagnostics applied to a millisecond pulsed-dc hybrid discharge in atmospheric pressure air. Plasma Chem Plasma Process. https://doi.org/10.1007/s11090-022-10233-7
5. Raizer Y (1991) Gas discharge physics. Springer, Berlin
6. Bruggeman PJ, Iza F, Brandenburg R (2017) Foundations of atmospheric pressure non-equilibrium plasmas. Plasma Sources Sci Technol. https://doi.org/10.1088/1361-6595/aa97af
7. Cernak M, Hoder T, Bonaventura Z (2019) Streamer breakdown: cathode spot formation, Trichel pulses and cathode-sheath instabilities. Plasma Sources Sci Technol. https://doi.org/10.1088/1361-6595/ab5051
8. Kunhardt EE (2000) Generation of large-volume, atmospheric-pressure, nonequilibrium plasmas. IEEE Trans Plasma Sci. https://doi.org/10.1109/27.842901
9. Staack D, Farouk B, Gutsol A, Fridman A (2009) Stabilization of the ionization overheating thermal instability in atmospheric pressure microplasmas. J Appl Phys. https://doi.org/10.1063/1.3143781
10. Akishev Y, Grushin M, Karalnik V, Petryakov A, Trushkin N (2010) Non-equilibrium constricted dc glow discharge in $N_2$ flow at atmospheric pressure: stable and unstable regimes. J Phys D Appl Phys. https://doi.org/10.1088/0022-3727/43/7/075202
11. Gnybida M, Loffhagen D, Uhrlandt D (2009) Fluid modeling and analysis of the constriction of the DC positive column in argon. IEEE Trans Plasma Sci. https://doi.org/10.1109/tps.2009.2021419
12. Shneider MN, Mokrov MS, Milikh GM (2012) Dynamic contraction of the positive column of a self-sustained glow discharge in molecular gas. Phys Plasmas. https://doi.org/10.1063/1.3694913
13. Shneider MN, Mokrov MN, Milikh G (2013) Dynamic contraction of the positive column of a self-sustained glow discharge in nitrogen/air flow. AIAA. https://doi.org/10.2514/6.2013-1186
14. Shneider MN, Mokrov MS, Milikh GM (2014) Dynamic contraction of the positive column of a self-sustained glow discharge in air flow. Phys Plasmas. https://doi.org/10.1063/1.4869332

15. Saifutdinov AI (2021) Unified simulation of different modes in atmospheric pressure DC discharges in nitrogen. J Appl Phys. https://doi.org/10.1063/5.0033372
16. Cejas E, Prevosto L, Minotti FO, Ferreyra M, Chamorro JC, Fina B (2021) Cathode-sheath model for field emission sustained atmospheric pressure discharges. Phys Plasmas. https://doi.org/10.1063/5.0035710
17. Naidis GV (2007) Simulation of convection-stabilized low-current glow and arc discharges in atmospheric-pressure air. Plasma Sources Sci Technol. https://doi.org/10.1088/0963-0252/16/2/012
18. Sakiyama Y, Graves DB, Chang H-W, Shimizu T, Morfill GE (2012) Plasma chemistry model of surface microdischarge in humid air and dynamics of reactive neutral species. J Phys D Appl Phys. https://doi.org/10.1088/0022-3727/45/42/425201
19. Capitelli M, Ferreira CM, Gordiets BF, Osipov AI (2000) Plasma kinetics in atmospheric gases. Springer, New York
20. Viehland LA, Mason EA (1995) Transport properties of gaseous ions over a wide energy range IV. At Data Nucl Data Tables 60(1):37–95. https://doi.org/10.1006/adnd.1995.1004
21. Nelson D, Benhenni M, Eichwald O, Yousfi M (2003) Ion swarm data for electrical discharge modeling in air and flue gas mixtures. J Appl Phys. https://doi.org/10.1063/1.1582232
22. Boissonnat G, Fontbonne JM, Colin J, Remadi A, Salvador S (2016) Measurement of ion and electron drift velocity and electronic attachment in air for ionization chambers. https://doi.org/10.48550/arXiv.1609.03740
23. Benilov MS, Naidis GV (2003) Modelling of low-current discharges in atmospheric-pressure air taking account of non-equilibrium effects. J Phys D Appl Phys. https://doi.org/10.1088/0022-3727/36/15/314
24. Popov NA (2011) Fast gas heating in a nitrogen–oxygen discharge plasma: I. Kinetic mechanism. J Phys D Appl Phys. https://doi.org/10.1088/0022-3727/44/28/285201
25. Popov NA (2001) Investigation of the mechanism for rapid heating of nitrogen and air in gas discharges. Plasma Phys Rep. https://doi.org/10.1134/1.1409722
26. D'Angola A, Colonna G, Bonomo A, Bruno D, Laricchiuta A, Capitelli M (2012) A phenomenological approach for the transport properties of air plasmas. Eur Phys J D. https://doi.org/10.1140/epjd/e2012-30147-8
27. Akishev Y, Grushin M, Karalnik V, Petryakov A, Trushkin N (2010) On basic processes sustaining constricted glow discharge in longitudinal $N_2$ flow at atmospheric pressure. J Phys D Appl Phys. https://doi.org/10.1088/0022-3727/43/21/215202
28. Lowke JJ (1979) Simple theory of free-burning arcs. J Phys D Appl Phys. https://doi.org/10.1088/0022-3727/12/11/016
29. Hagelaar GJM, Pitchford LC (2005) Plasma Sources. Sci Technol 14:722–733
30. Zhong H, Mao X, Mokrov MS, Shneider MN, Ju Y (2022) 2D modeling of plasma dynamic contraction in the positive column of glow discharge. AIAA SCITECH 2022 Forum. https://doi.org/10.2514/6.2022-1109
31. Aleksandrov NL, Bazelyan EM, Kochetov IV, Dyatko NA (1997) The ionization kinetics and electric field in the leader channel in long air gaps. J Phys D Appl Phys. https://doi.org/10.1088/0022-3727/30/11/011
32. SIGLO. Database. Accepted on 5, 2022.Available online: http://www.lxcat.laplace.univ-tlse.fr
33. MORGAN. Database. Accepted on 5, 2022. Available online: www.lxcat.net
34. Losev S, Makarov V, Nikolsky V (1994) Thermochemical nonequilibrium kinetic models in strong shock waves on air. In: 6th joint thermophysics and heat transfer conference. https://doi.org/10.2514/6.1994-1990
35. Da Silva ML, Guerra V, Loureiro J (2007) Two-temperature models for nitrogen dissociation. Chem Phys. https://doi.org/10.1016/j.chemphys.2007.10.01
36. Kang S-W, Jones WL, Dunn MG (1973) Theoretical and measured electron-density distributions at high altitudes. AIAA J. https://doi.org/10.2514/3.50446
37. Lin S-C, Teare JD (1963) Rate of ionization behind shock waves in air. II Theor Interpret Phys Fluids. https://doi.org/10.1063/1.1706741
38. Makarov VN (1996) Determination of the mechanism of physicochemical processes in high-temperature air. J Appl Mech Tech Phys. https://doi.org/10.1007/BF02382426
39. Park C (1989) A review of radiation rata in high. Temperature air. In: 24th thermophysics conference. https://doi.org/10.2514/6.1989-1740
40. Kossyi IA, Kostinsky AY, Matveyev AA, Silakov VP (1992) Kinetic scheme of the non-equilibrium discharge in nitrogen-oxygen mixtures. Plasma Sources Sci Technol. https://doi.org/10.1088/0963-0252/1/3/011

41. Fletcher CAJ (1991) Computational techniques for fluids dynamics. Fundamental and general techniques. Springer, Cham
42. Scharfetter DL, Gummel HK (1969) Large-signal analysis of a silicon read diode oscillator. IEEE Trans Electron Devices. https://doi.org/10.1109/t-ed.1969.16566
43. Kulikovsky AA (1995) A more accurate scharfetter-gummel algorithm of electron transport for semiconductor and gas discharge simulation. J Comput Phys. https://doi.org/10.1006/jcph.1995.1123
44. Gambling WA (1953) Glows, arcs, and glow-to-arc transitions. SQJ. https://doi.org/10.1049/sqj.1953.0045
45. Gambling WA, Edels H (1954) The high-pressure glow discharge in air. Br J Appl Phys. https://doi.org/10.1088/0508-3443/5/1/309
46. Mezei P, Cserfalvi T, Janossy M (2001) On the pressure dependence of the positive column cross section in high-pressure glow discharges. J Phys D Appl Phys. https://doi.org/10.1088/0022-3727/34/12/323
47. Akishev Y, Karalnik V, Kochetov I, Napartovich A, Trushkin N (2014) High-current cathode and anode spots in gas discharges at moderate and elevated pressures. Plasma Sources Sci Technol. https://doi.org/10.1088/0963-0252/23/5/054013
48. Fridman A, Kennedy L (2004) Plasma physics and engineering. Taylor & Francis, New York
49. Xiong Q, Xu L, Wang X, Xiong L, Huang Q, Chen Q, Wang J, Peng W, Li J (2018) Full spatial-field visualization of gas temperature in an air micro-glow discharge by calibrated Schlieren photography. J Phys D Appl Phys. https://doi.org/10.1088/1361-6463/aaa882
50. Gamaleev V, Tsutsumi T, Hiramatsu M, Ito M, Hori M (2020) Generation and diagnostics of ambient air glow discharge in centimeter-order gaps. IEEE Access. https://doi.org/10.1109/ACCESS.2020.2988091
51. Stepaniuk VP, Ioppolo T, Ötügen MV, Sheverev VA (2007) Measurement of gas temperature and convection velocity profiles in a DC atmospheric glow discharge. J Appl Phys. https://doi.org/10.1063/1.2822338
52. Gleizes A, Gonzalez JJ, Freton P (2005) Thermal plasma modelling. J Phys D Appl Phys. https://doi.org/10.1088/0022-3727/38/9/r01
53. Lu X, Leipold F, Laroussi M (2003) Optical and electrical diagnostics of a non-equilibrium air plasma. J Phys D Appl Phys. https://doi.org/10.1088/0022-3727/36/21/011
54. Stark RH, Schoenbach KH (1999) Direct current glow discharges in atmospheric air. Appl Phys Lett. https://doi.org/10.1063/1.124174
55. Leipold F, Stark RH, El–Habachi A, Schoenbach KH, (2000) Electron density measurements in an atmospheric pressure air plasma by means of infrared heterodyne interferometry. J Phys D Appl Phys. https://doi.org/10.1088/0022-3727/33/18/310
56. Machala Z, Marode E, Laux CO, Kruger CH (2004) DC glow discharges in atmospheric pressure air. J Adv Oxid Technol. https://doi.org/10.1515/jaots-2004-0206
57. Gordiets BF, Ferreira CM, Guerra VL, Loureiro JMAH, Nahorny J, Pagnon D, Touzeau M, Vialle M (1995) Kinetic model of a low-pressure $N_2$–$O_2$ flowing glow discharge. IEEE Trans Plasma Sci. https://doi.org/10.1109/27.467998